doi:10.1038/nature09771

In these Supplemental Notes to our main paper, we outline key details related to how we estimated the angular power spectrum of *Herschel*-SPIRE data and its interpretation.

The data presented in the main paper are publicly available from the ESA/Herschel Science Archive (http://herschel.esac.esa.int) under the observational identifications 1342186108, 1342186109, and 1342185536. Derived products by the HerMES collaboration, such as source catalogs, will be released through the HeDaM Database (http://hedam.oamp.fr/HerMES).

Data Analysis and Map making: The data were taken in the standard Scan-Map AOT for which the scanning speed is 30"/s. Calibrated time-ordered data were created using HIPE[31] development version 2.0.905, with a fix applied to the astrometry (included in more recent versions of the pipeline), with newer calibration files (SPIRE Beam Steering Mirror calibration version 2, flux conversion version 2.3 and temperature drift correction version 2.3.2) and with a median slope subtracted from each timeline. We removed a few percent of the data samples which were contaminated by cosmic-rays or instrumental effects and flagged by the initial pipeline.

We convert time-ordered data to a map on the sky through an iterative baseline removal and an iterative calculation of detector weights. We give a summary of the map-making method here. Full details of this approach is available elsewhere[32,34].

Given sky brightness $I(\theta)$, the signal for a detector d in a scan s with a time sample j can be written as

$$S_{dsj} = I(\theta_{dsj}) + P^n_{ds} + N_{dsj}\,, \tag{1}$$

where P^n_{ds} is an n-th order polynomial baseline offset for detector d and scan s, and N_{dsj} is the instrumental noise. The parameters of P^n_{ds} are solved with an iterative solution to the best-intensity of the sky at each step.

At each iteration i, we minimize the variance of the residual V^i_{dsj} based on the previous map $I^{i-1}(\theta_{dsj})$ such that

$$V^i_{dsj} = S_{dsj} - \left[I^{i-1}(\theta_{dsj}) + P^{n,i}_{ds}\right]\,. \tag{2}$$

The i-th estimate of the sky is performed via the weighted mean of all the samples that fall into a given pixel:

$$I^i(\theta) = \frac{\sum_{dsj} w^i_{ds}\left(S_{dsj} - P^{n,i}_{ds}\right)}{\sum_{dsj} w^i_{ds}}\,. \tag{3}$$

The weight associated with each iterative estimate is simply the inverse variance of the residual

$$w^i_{ds} = \frac{N_{\rm tot}}{\sum_{k=1}^{N_{\rm tot}}\left(V^i_{dsj}\right)^2}\,. \tag{4}$$

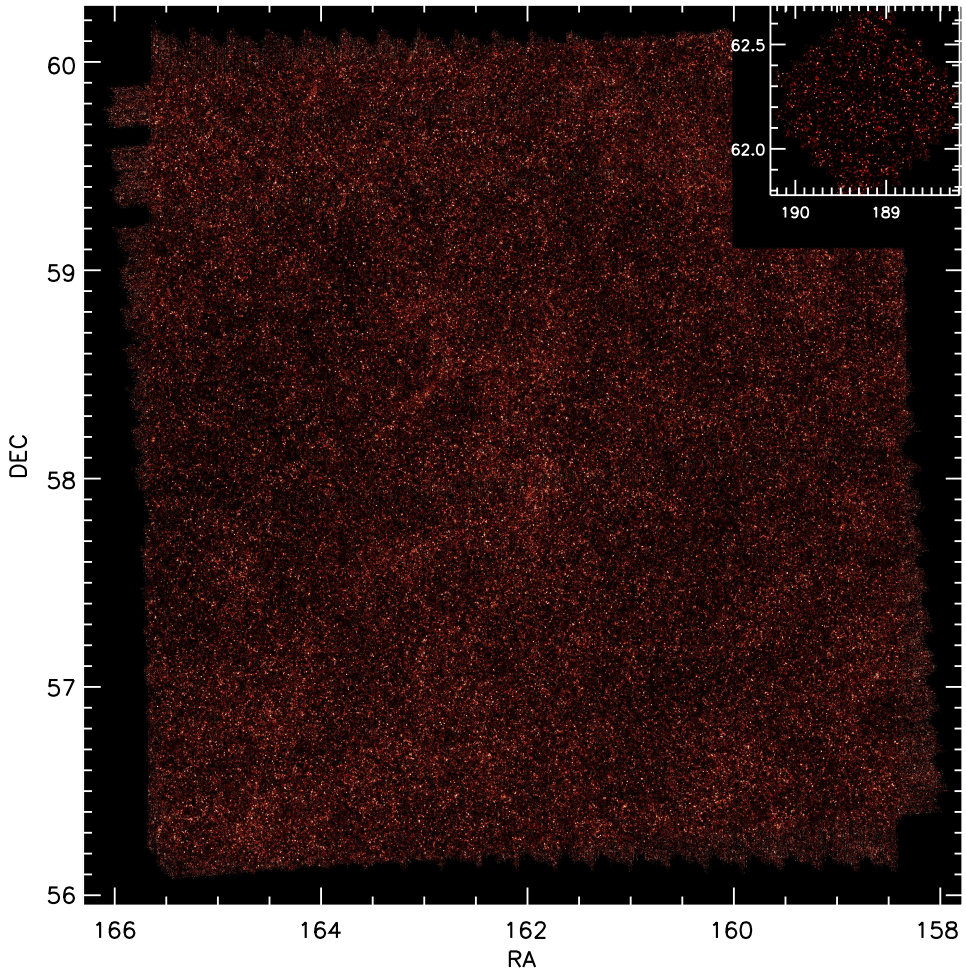

Figure S 1: **The 250 μm SPIRE maps of Lockman-SWIRE and GOODS-N (top-right inset) fields.** We have masked all galaxies above 50 mJy.

The algorithm also allows us to create a noise map by propagating detector noise as estimated by the variance of the residuals. The maps used here make use of a first-order polynomial with $n = 1$ and 20 iterations. The gain offsets were computed from the 1st iteration while the weights are fixed to 1.0 for the 10 iterations and are calculated from the data starting at iteration 11, to improve stability of the algorithm. The same procedure is repeated for both Lockman-SWIRE and GOODS-N maps and also iterative maps of Neptune that we use for beam measurements. The maps at 250 μm are shown in Figure S1.

The absolute astrometry of the maps was corrected by stacking at the positions of *Spitzer* Multi-Band Imaging Photometer (MIPS) 24 μm and radio sources, finding reasonably consistent results between the two within 0.5″. We have made an overall correction to the absolute astrometry of the order of a few arcseconds, though such small angular scale corrections do not impact results we present here focusing between 0.5 arcminutes to 100 arcminutes.

The maps were made with pixels of size 6, 8.3, and 12 arcseconds at 250, 350, 500 μm, respectively, corresponding to one third of the full-width at half-maximum (FWHM) of the SPIRE beam profiles[33] in the three passbands.

Raw Power Spectra To compute the power spectrum in our map, we use fast Fourier transforms; however, we need to take into account the missing and unwanted pixels. Due to our scanning strategy and some corrupted data, a small fraction of pixels are not defined on the map that we use to define our Fourier transform basis. Furthermore, we wish to remove the brightest galaxies in order to reduce the shot-noise term in the power spectrum, since the shot-noise term is weighted towards bright galaxies and larger shot-noise degrades the ability to extract the clustering component of the power spectrum. In our analysis we applied a flux cut of 50 mJy/beam, removing 0.9, 0.7, 1.2% of the pixels at 250, 350, 500 μm, respectively, in the Lockman-SWIRE field and 0.5, 0.2, 0.2% in the GOODS-N field. We used the same flux cut at all frequencies for simplicity, this 50 mJy/beam allows to remove all the bright sources while retaining most of the pixels in each map. The remaining number of pixels used for the fluctuation study is 5.4×10^6 , 2.9×10^6, and 1.4×10^6 at 250, 350, 500 μm, respectively, in the Lockman-SWIRE field and 1.9×10^5, 1.0×10^5, 4.7×10^4 in the GOODS-N field.

The raw power spectra are summarized in Figure S2. Here, we show the auto spectra in the total map as well as the cross spectrum with maps made with half of the time-ordered data in each map. The difference of the two provides us with an estimate of the instrumental noise. At small physical scales (large k values) the noise is almost white such that $P(k)$ is a constant value. We fit a model of the form

$$N(k) = N_0 \left[\left(\frac{k_0}{k} \right)^2 + 1 \right] , \quad (5)$$

and determine the knee scale of the noise, k_0, to be at about 0.15 arcmin^{-1} at each of 250, 350, and 500 μm.

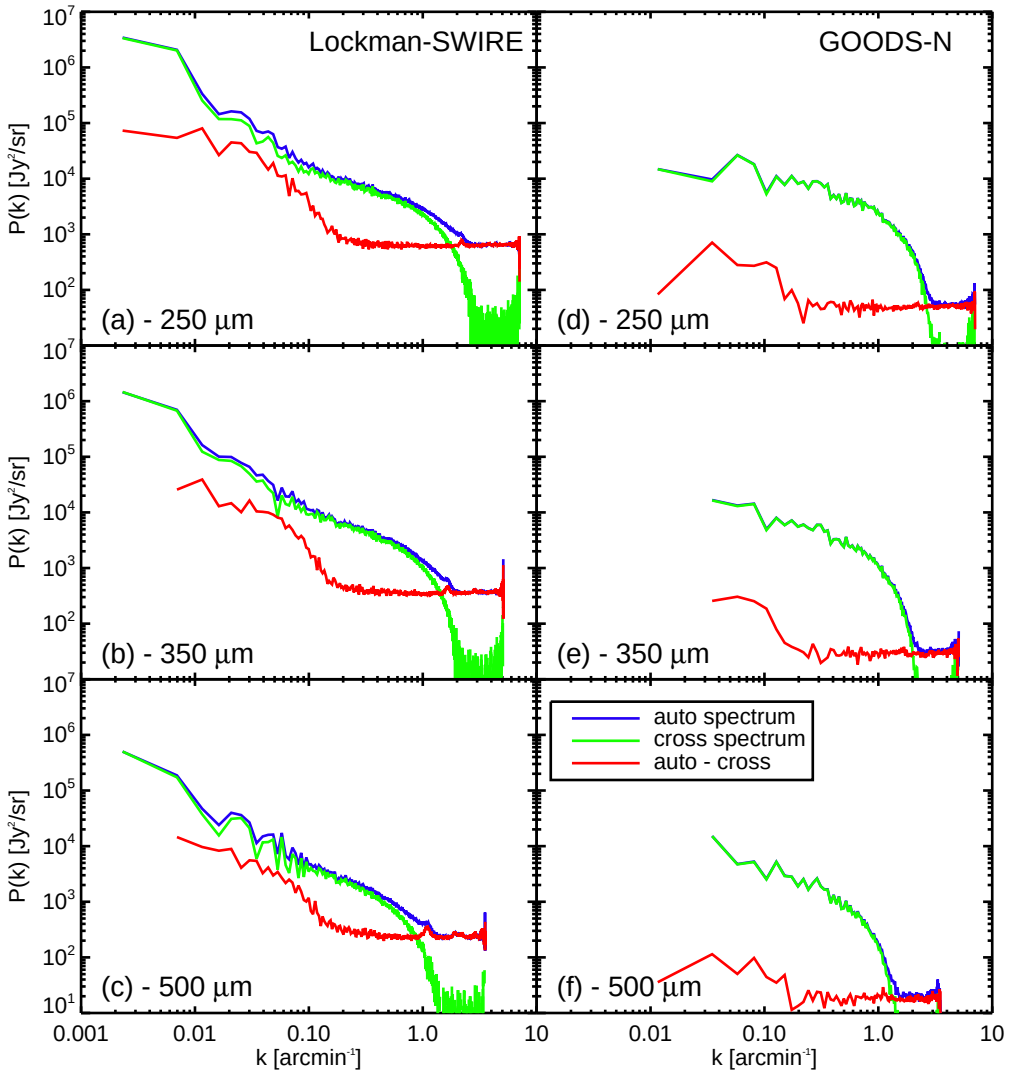

Figure S 2: **Raw $P(k)$ of the Lockman-SWIRE (left) and GOODS-N (right) fields.** The panels show the three wavebands with 250 μm (panels *a* and *d*), 350 μm (*b* and *e*), and 500 μm (*c* and *f*) from top to bottom on each side, respectively. The blue lines show the auto-power spectra computed from maps using all the data. This power spectrum is a combination of sky signal and instrumental noise. We estimate the sky signal through the cross-spectrum (green lines) of two maps after dividing the data into two halves separated in time. The difference of these two spectra represents an estimate of the instrumental noise power spectrum (red line).

P(k) - 250 μm		P(k) - 350 μm		P(k) - 500 μm	
k [arcmin^{-1}]	P(k) [Jy^2/sr]	k [arcmin^{-1}]	P(k) [Jy^2/sr]	k [arcmin^{-1}]	P(k) [Jy^2/sr]
0.046	31301 $\pm$ 11721	0.021	34368 $\pm$ 28830	0.021	24279 $\pm$ 10312
0.056	12974 $\pm$ 6796	0.025	39732 $\pm$ 19767	0.025	29273 $\pm$ 8420
0.065	15266 $\pm$ 4974	0.030	29473 $\pm$ 14296	0.030	16617 $\pm$ 5009
0.076	12678 $\pm$ 3247	0.035	24589 $\pm$ 9973	0.037	7264 $\pm$ 1803
0.090	12098 $\pm$ 2290	0.042	26510 $\pm$ 6130	0.044	11644 $\pm$ 2837
0.104	12911 $\pm$ 1740	0.049	17856 $\pm$ 5430	0.049	12368 $\pm$ 2538
0.120	11587 $\pm$ 1212	0.056	11270 $\pm$ 2808	0.056	9265 $\pm$ 1376
0.141	11538 $\pm$ 870	0.065	12359 $\pm$ 2226	0.065	3787 $\pm$ 652
0.164	9466 $\pm$ 637	0.076	14499 $\pm$ 1638	0.076	5580 $\pm$ 584
0.190	9672 $\pm$ 502	0.090	10482 $\pm$ 1099	0.088	4724 $\pm$ 533
0.220	9744 $\pm$ 412	0.104	9476 $\pm$ 831	0.100	4637 $\pm$ 386
0.257	8305 $\pm$ 299	0.120	8808 $\pm$ 599	0.116	3980 $\pm$ 269
0.299	8096 $\pm$ 258	0.139	8611 $\pm$ 506	0.134	3702 $\pm$ 226
0.345	7853 $\pm$ 212	0.160	8312 $\pm$ 406	0.153	3575 $\pm$ 209
0.400	7185 $\pm$ 162	0.185	6663 $\pm$ 288	0.174	3014 $\pm$ 159
0.465	6787 $\pm$ 126	0.213	6844 $\pm$ 272	0.199	3012 $\pm$ 145
0.539	6777 $\pm$ 115	0.245	6423 $\pm$ 217	0.229	2707 $\pm$ 125
0.625	6576 $\pm$ 105	0.285	6183 $\pm$ 185	0.262	2632 $\pm$ 121
0.725	6463 $\pm$ 99	0.329	5677 $\pm$ 152	0.299	2383 $\pm$ 104
0.840	6358 $\pm$ 100	0.377	5289 $\pm$ 134	0.343	2335 $\pm$ 98
0.975	6417 $\pm$ 107	0.435	4950 $\pm$ 115	0.391	2195 $\pm$ 88
1.130	6206 $\pm$ 115	0.502	5098 $\pm$ 112	0.447	2148 $\pm$ 84
1.310	6093 $\pm$ 135	0.579	4994 $\pm$ 104	0.512	2136 $\pm$ 83
1.519	6197 $\pm$ 162	0.667	4878 $\pm$ 98	0.586	2029 $\pm$ 80
1.757	6094 $\pm$ 200	0.766	4768 $\pm$ 94	0.669	1967 $\pm$ 82
2.035	6080 $\pm$ 243	0.882	4726 $\pm$ 94	0.764	1934 $\pm$ 82
2.356	6161 $\pm$ 332	1.016	4736 $\pm$ 95	0.875	1997 $\pm$ 91
2.729	6604 $\pm$ 535	1.169	4574 $\pm$ 97	1.000	1910 $\pm$ 94
		1.345	4586 $\pm$ 104	1.141	1871 $\pm$ 109
		1.549	4609 $\pm$ 121		

Table S 1: **P(k) measured on Lockman-SWIRE field**.

Notes: The values correct for all known effects (beam, map-making transfer function, Galactic cirrus) with error bars at the 3 SPIRE frequencies.

Corrected Power Spectra: The final power spectrum we show in this paper (and tabulated in Table) is corrected for a combination of effects described by

$$P(k') = B(k)T(k)M_{k'k}P(k)\,, \tag{6}$$

where $P(k')$ is the observed power spectrum from data in the presence of mask, $B(k)$ is the beam function, and the map making transfer function is $T(k)$. $P(k)$ is the true sky power spectrum and is determined by inverting the above equation.

In the above, $M_{kk'}$ is the mode coupling matrix associated with the mask. This can be expressed analytically in the flat sky approximation[35] as

$$M_{kk'} = \sum_{\theta_k}\sum_{\theta_{k'}} |w(k-k')|^2/N(\theta_k)\,, \tag{7}$$

where $w(k)$ is the Fourier transform of the mask. Figure S3 shows the mask we used and the corresponding matrix $M_{kk'}$ for each of Lockman-SWIRE and GOODS-N fields at 250 μm with sources above 50 mJy and spurious data removed.

We measure the beam function $B(k)$ through observations of Neptune, involving a total of 700 scans. Figure S4 shows the Neptune maps made at 250, 350, and 500 μm. The Neptune data are analyzed in the same manner as the Lockman-SWIRE and GOODS-N data using the same iterative map maker. In addition we also employ a naive map maker available as part of HIPE[31]. When making these maps, we account for the relative motion of Neptune relative to the background sky and make maps that correct for Neptune's varying position during the observations. This results in a map where extragalactic sources are smeared. Neptune, however, is several orders of magnitude brighter and our beam measurements primarily focus on the central region. Figure S5 summarizes the results related to $B(k)$ for each of the three SPIRE wavelengths. In the same figure (bottom panels), we also compare the beam measured from Neptune to the beam described by a Gaussian with a FWHM of 18, 25, and 36″ at 250, 350, and 500 μm. The amplitude of $B(k)$ is thereafter interpolated in the k modes at which we compute our fluctuation power spectra.

The uncertainty in the beam function $B(k)$ is determined by computing the standard deviation of the different $B(k)$ estimates, using the measurements on the iterative and naive map and several different interpolation schemes. The beam uncertainty computed this manner is slightly larger than the difference in the beams between two different observations of Neptune, one involving the fine scans we primarily use here and an older coarse set of Neptune scans, but with maps made using the same map-maker. Figure S6 shows the overall uncertainties in the beam (solid lines) as well as the uncertainties coming from the difference between the naive and iterative map reconstructions (dashed lines). Figure S7 compares the beam function and the power spectrum $P(k)$ at 250 μm from the Lockman-SWIRE field showing that features in the power spectrum are not related to features in the beam function $B(k)$.

To measure the transfer function $T(k)$ associated with the map maker, we realize 100 simu-

lations of a first estimate of our beam-convolved power spectrum and pass it through the iterative map-making pipeline used to reduce our real data. We then compute the average of the ratio between the estimated spectrum and the input spectrum with simulated maps masked exactly as in the real sky maps. This function is the transfer function $T(k)$ of the map-making pipeline associated with median filter and other filtering (Figure S8). We divide the estimated power spectrum by this transfer function to remove the map making pipeline processing effects.

Total error budget: The total error budget in our clustering plots is composed of three contributions involving the uncertainty of the beam, uncertainty in the shot-noise determination, and the instrumental noise error. The latter is computed from simulations while the beam error comes from the differences in our estimates of the beam. Shot-noise error results from direct fits to the measured data points. Figure S9 summarizes the error budget as a function of wave number and also compares the instrumental noise error to an analytical formula for its expectation[36].

While in Figure 1 of the main paper we showed $P(k)$ at 350 μm, in Figure S10 we show the same at 250 and 500 μm.

Jack-knife tests: The results shown in this study were obtained by dividing the data into two equal and consecutive halves and by taking the cross-power spectrum of the resultant maps. We can make the same cross-correlation power spectrum measurements and repeat the whole process with maps made by dividing data into several other combinations. To be specific, we divide the data into four pieces, each filling approximately our total field, and use these to measure the cross-power spectrum for two other combinations namely $[(1+3)\times(2+4)]$ and $[(1+4)\times(2+3)]$, where 1 to 4 are four equal subdivisions of data in time.

Figure S11 summarizes our results, showing that within the uncertainties we recover similar power spectra. Given the observing strategy, the $(1+3)$ and $(2+4)$ maps are each made with parallel scans, but roughly perpendicular to each other. The fact that we do not see a statistically significant difference shows that the beam ellipticity is not an important systematic concern in this study.

Null tests: In addition to the jack-knife tests with a variety of sub-maps with data divided to four intervals and all leading to a measurement of the sky signal, we also perform several null tests using data combinations that remove the sky signal. In this case, instead of computing the cross-power spectra of the sum maps of data combinations, we make use of the sub-maps made by taking the differences of data combinations, again data divided to four sub-intervals as the case of signal measurement. As an example, in Figure S12 we show the cross-power spectrum computed at 250, 350, and 500 μm with the $(1-2)$ map cross-correlated against the $(3-4)$ map. For reference, we also show the default power spectrum computed with $[(1+2)\times(3+4)]$.

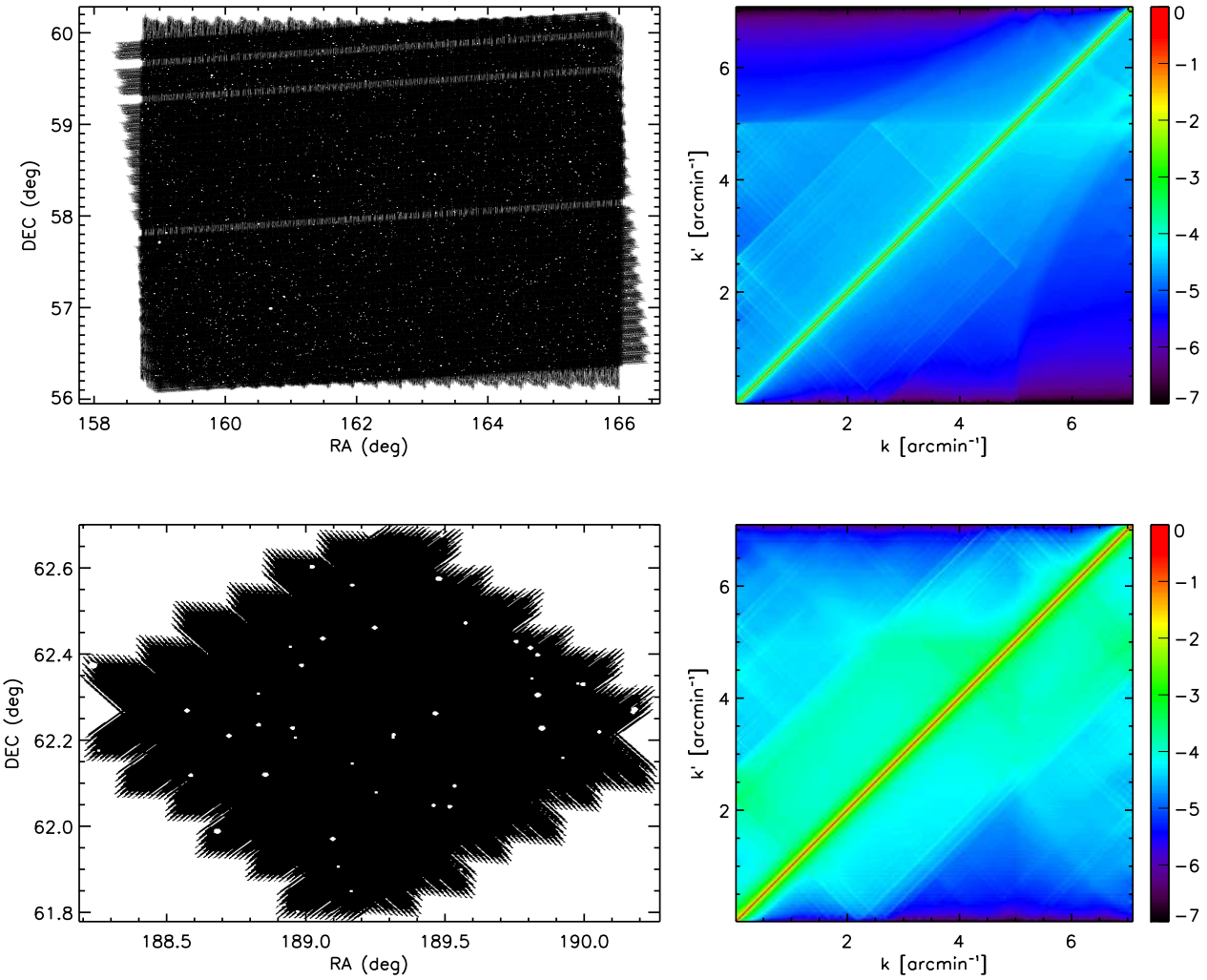

Figure S 3: **Mask and the model coupling matrix.** *Top-left :* Mask used for the Lockman-SWIRE field. The galaxies brighter than 50 mJy masked as well as some corrupted scans. *Top-right:* Coupling matrix $M_{kk'}$ (log scale) computed for this Lockman-SWIRE mask. Bottom-left and bottom-right figures are the same things for the GOODS-N field.

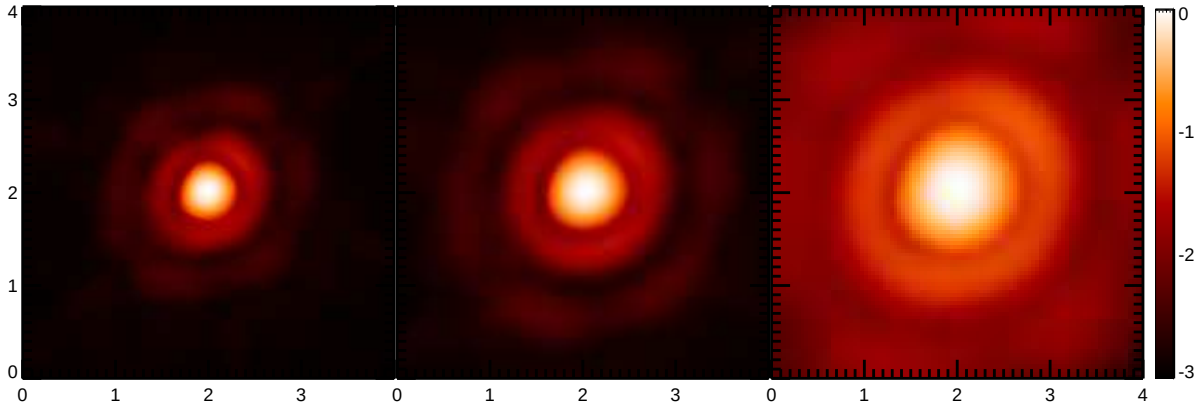

Figure S 4: **Maps used for the beam function measurements.** From left to right, Neptune beam maps (log scale normalized to the maximum) at 250, 350, and 500 μm, respectively. The x- and y-axes are labeled in arcminutes. The maps were made with the iterative map-maker and observations involve a total of 700 scans of Neptune.

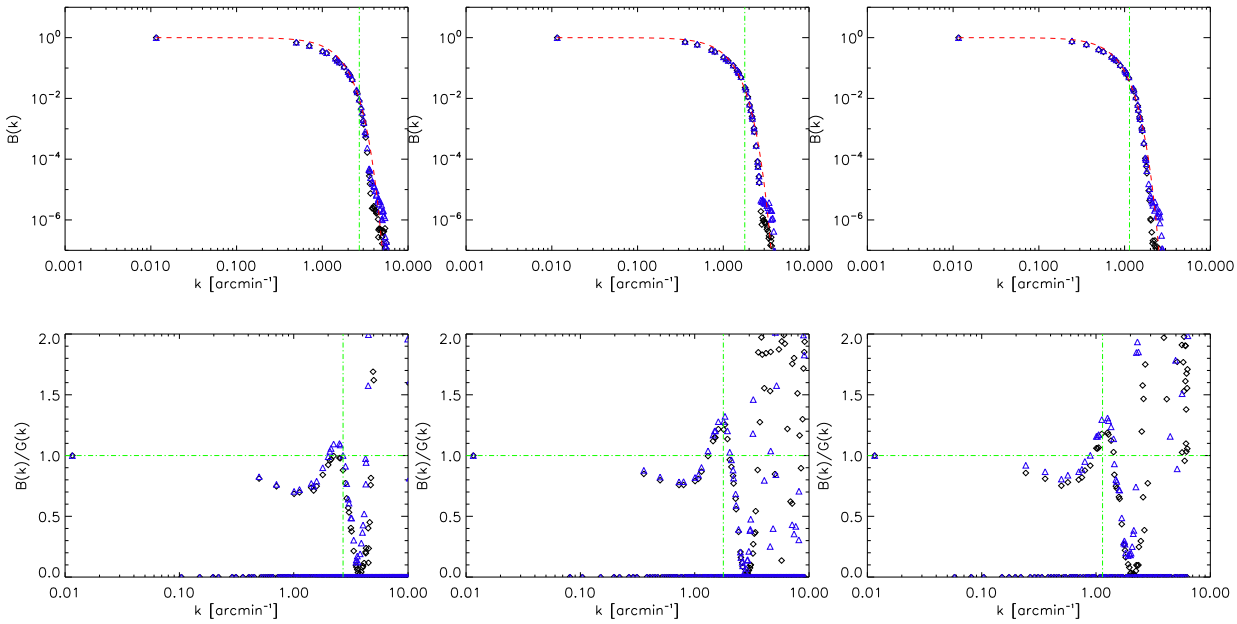

Figure S 5: **Point spread function of SPIRE Instrument**. **Top :** Point Spread Function Fourier space kernels for 250, 350 and 500 μm (from left to right). The black diamonds were estimated using the Neptune "naive" map, the blue triangles with the Neptune "iterative" map and the red dashed line is the Gaussian (FWHM of 18, 25 and 36 arcseconds). The vertical green dashed dotted lines represent the maximum k out to which the data are used in this analysis. **Bottom:** Ratio of the beam kernel measured on Neptune to the Gaussian beam approximation.

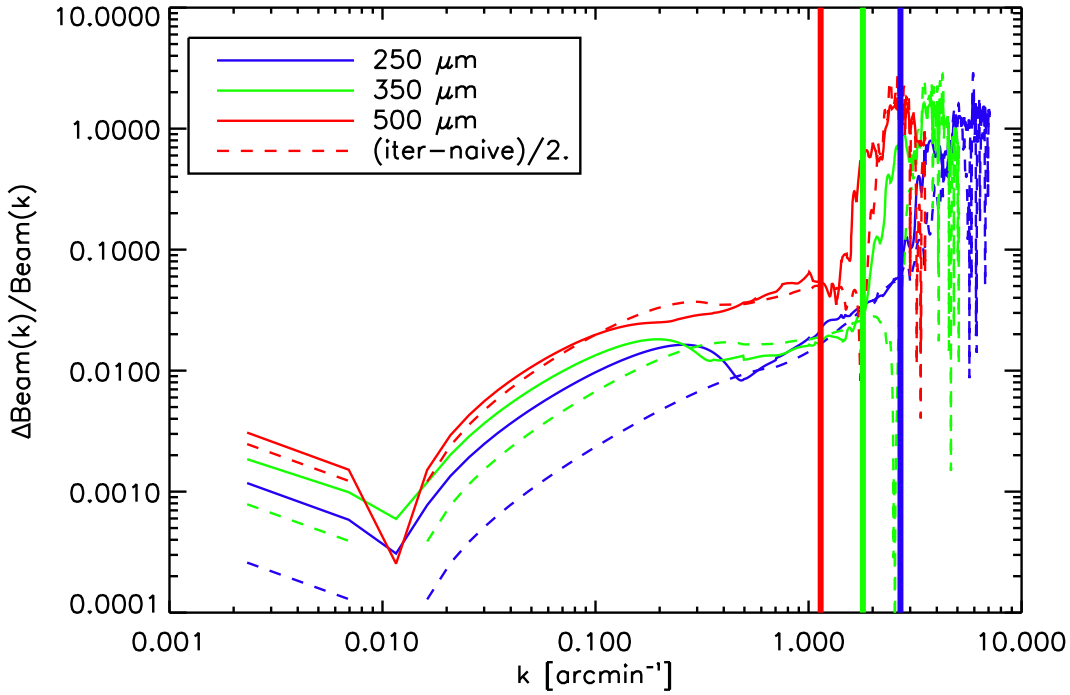

Figure S 6: **Accuracy of the beam measurement.** The beam uncertainty relative to the mean beam function used for this analysis. The total uncertainty (solid lines) is the standard deviation of the different $B(k)$ estimates using the measurements on the iterative and naive map and several interpolation methods. The dashed lines are half of the difference between one of the naive map $B(k)$ estimates and one of the iterative map $B(k)$ estimates. The vertical lines mark the maximum k value out to which we make use of the power spectrum measurements at each of 250, 350, and 500 μm.

Band	A (Jy^2/sr)	n	$P_{\rm SN}$ (Jy^2/sr)	χ^2/d.o.f.
250 μm	$(7.64 \pm 0.55) \times 10^3$	-1.20 ± 0.09	5798^{+92}_{-132}	0.93
350 μm	$(5.79 \pm 0.26) \times 10^3$	-1.28 ± 0.07	4373^{+62}_{-76}	1.03
500 μm	$(2.67 \pm 0.13) \times 10^3$	-1.16 ± 0.09	1700 ± 80	1.2

Table S 2: **Power-law best fit values at $k_1 = 0.1$ arcmin^{-1}.**

Notes: To describe the power spectrum, we take a power-law with $P(k) = A(k/k_1)^n + P_{\rm SN}$ where k_1 is fixed at 0.1 arcmin^{-1} and $P_{\rm SN}$ is the shot-noise amplitude, assuming a power-law fit to the data. The errors are 68% confidence level uncertainties determined from the MCMC fits.

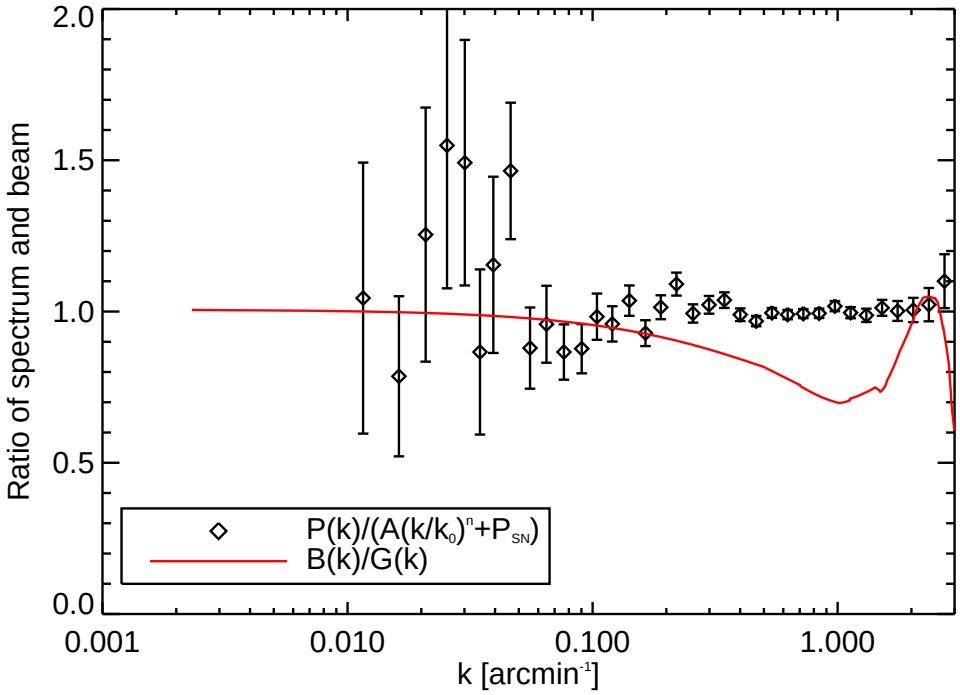

Figure S 7: **Power spectrum relative to the beam function**. Comparison of the $P(k)$ estimate and the beam transfer function shape. The black diamonds represent our 250 μm $P(k)$ estimate divided by the best fit power-law. The red line represents our beam transfer function divided by the approximate Gaussian beam. The two curves have different shapes and this difference indicates that the $P(k)$ shape does not come from the beam transfer function.

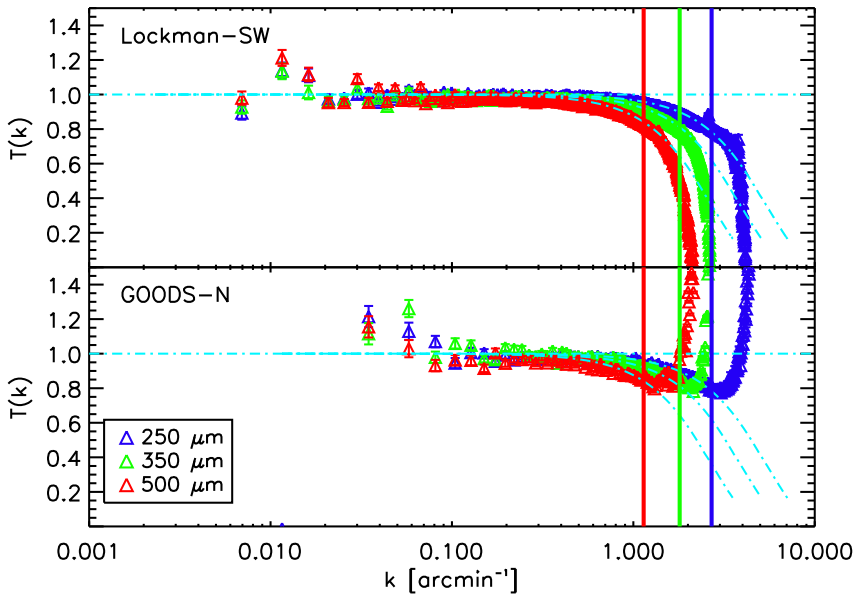

Figure S 8: **Map-making transfer function.** Transfer function $T(k)$ due to the iterative map-maker and filtering on the cross-spectra of our two fields. The blue, green and red triangles represent, respectively, the transfer function at 250, 350 and 500 μm. $T(k)$ is essentially equal to 1 between 0.02 and 0.4 arcmin^{-1}. The map-maker adds about 10% power around 0.01 arcmin^{-1} in the case of Lockman-SWIRE (top panel) and around 0.05 arcmin^{-1} in the case of GOODS-N (bottom panel) and reduces the power on small scales mostly by averaging the data into pixels (light blue dotted dashed lines). The vertical lines mark the maximum k out to which we make use of the power spectrum estimates for shot-noise and clustering measurements.

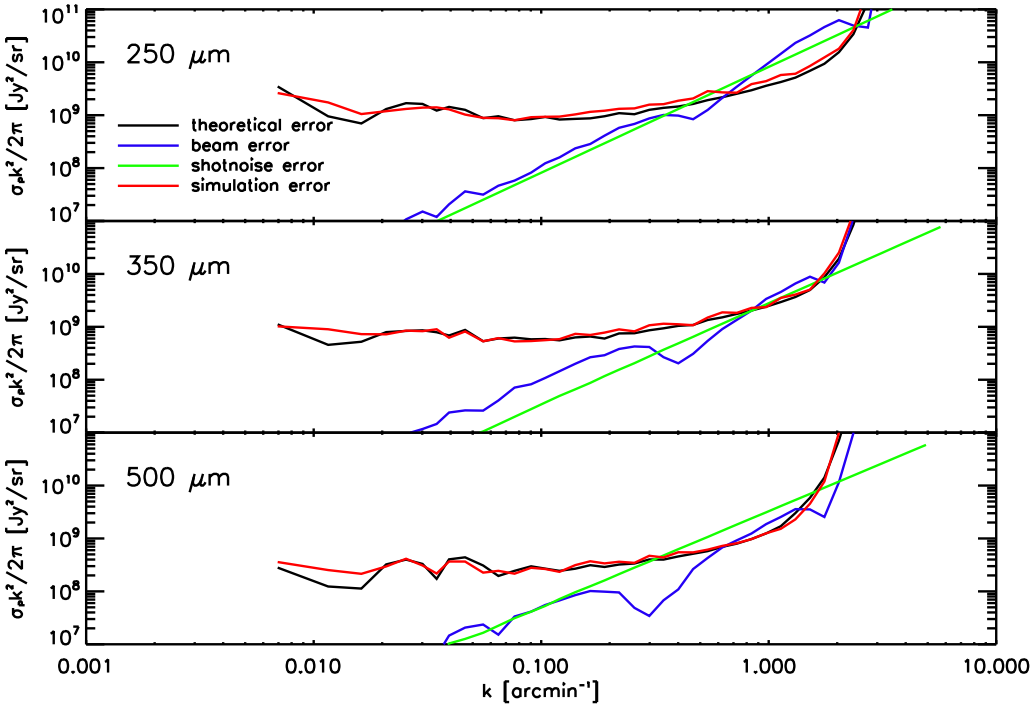

Figure S 9: **The power spectrum uncertainties.** Error budget at 250, 350, and 500 μm. We show the error separated into the beam uncertainty (blue lines), the shot-noise determination (green lines), and the simulations (sky and instrumental variance, red lines). The simulation uncertainty is compared to an analytical noise estimate (black lines).

Cirrus power spectrum The cirrus signal in our Lockman-SWIRE field is taken from existing measurements in the same field with *IRAS* 100 μm and MIPS[39] with a power spectrum, $P(k)$, of the form $P_{\rm cirrus}(k) = P_0(k/k_0)^{\beta}$ at 160 μm with $P_0 = (2.98 \pm 0.66) \times 10^6$ Jy^2/sr and $\beta = -2.89 \pm 0.22$ when $k_0 = 0.01$ arcmin^{-1}. We and extend this spectrum from 100 μm to SPIRE wavelengths using the spectral dependence of a Galactic dust model[40].

	$log[M_{\rm min}/M_{\odot}]$	α	$\langle b \rangle_z$	$P_{\rm SN}$ (Jy^2/sr)	χ^2/d.o.f.
250 μm	$11.1^{+1.0}_{-0.6}$	$1.6^{+0.1}_{-0.2}$	$2.0^{+0.9}_{-0.1}$	6100 ± 120	0.76
350 μm	$11.5^{+0.7}_{-0.2}$	$1.8^{+0.1}_{-0.7}$	$2.4^{+1.0}_{-0.2}$	4600 ± 70	1.02
500 μm	$11.8^{+0.4}_{-0.3}$	$1.8^{+0.1}_{-0.7}$	$2.8^{+0.4}_{-0.5}$	1800 ± 80	1.44

Table S 3: **Halo model best fit values from the measured power spectra at the three wavebands.**

We tabulate the best-fit values with 68% confidence level errors for halo occupation number used to interpret the power spectrum measurements. The average galaxy bias factor is $\langle b \rangle_z$. $P_{\rm SN}$ is the amplitude of shot-noise fluctuations, also jointly determined from the power spectra as part of our model fitting process. The errors of the shot-noise amplitudes $P_{\rm SN}$ include an extra error corresponding to the uncertainty of the absolute flux calibration scale at the three SPIRE wavebands of 15%[33]. The chi-square values of the best-fit model, per degree-of-freedom, are also tabulated. We do not tabulate the values of M_1 as it remains unconstrained within the prior of $M_1/M_{\rm min}$ taken to be between 10 and 25.

Interpretation Model In Table S2 we summarize results related to power-law model fits with $P(k) = A(k/k_1)^n + P_{\rm SN}$, where $k_1 = 0.1$ arcmin^{-1}. We also make use of the halo model approach to model-fit our clustering measurements, making use of the halo occupation distribution (HOD)[41].

The number of pairs of galaxies inside a given halo depends on the variance of the HOD, $\sigma^2(M,z) = \langle N_{\rm gal}(N_{\rm gal}-1)\rangle$ while the number of pairs of galaxies in different halos is simply given by the square of the mean halo occupation with $N(M,z) = \langle N_{\rm gal}\rangle$, where $N_{\rm gal}$ is the total number of galaxies in a halo and we further assume that one galaxy occupies the center of the halo, the others being considered as satellite galaxies, so that $N_{\rm gal} = N_{\rm cen} + N_{\rm sat}$. Central and satellite galaxies are assumed to have different HODs; in fact the mean number of central galaxies in a given halo is a simple step function, so that $N_{\rm cen} = 1$ above a given mass $M_{\rm min}$, and $N_{\rm cen} = 0$ otherwise. The HOD of satellite galaxies is taken to be a power law of the halo mass[42]:

$$N_{\rm sat} = \left(\frac{M}{M_1}\right)^{\alpha}; \tag{8}$$

here M_1 is a normalization factor that represents the mass scale at which a single halo hosts on average one satellite galaxy in addition to the central galaxy.

The power spectrum of galaxies is then parameterized as the sum of two different contributions: the 1-halo term, which describes the clustering on small scales and is related to pairs of galaxies within the same halo and the 2-halo term, responsible for the large scale clustering and related to pairs of galaxies in different halos:

$$P(k,z) = P_{\rm 1h}(k,z) + P_{\rm 2h}(k,z). \tag{9}$$

The two terms are then written as:

$$\begin{aligned} P_{\rm 1h}(k,z) &= \int dM\, \frac{dn_{\rm halo}}{dM}(z)[2N_{\rm cen}(M)N_{\rm sat}(M)u_{\rm DM}(k,z|M) + \\ &\quad N^2_{\rm sat}(M)u^2_{\rm DM}(k,z|M)]dM/n^2_{\rm gal}(z), \\ P_{\rm 2h}(k,z) &= P_{\rm DM}(k,z) \times \\ &\quad \Big[\int dM\, \frac{dn_{\rm halo}}{dM}(z)N_{\rm gal}(M,z) \times \\ &\quad b(M,z)u_{\rm DM}(k,z|M)dM\Big]^2/n^2_{\rm gal}(z). \end{aligned} \tag{10}$$

Here $P_{\rm DM}(k,z)$ is the linear dark matter power spectrum; $n_{\rm halo}$ is the halo-mass function[43]; $b(M,z)$ is the linear bias which connects the large scale clustering of dark matter to the galaxy clustering; $u_{\rm DM}(k,z|M)$ is the normalized dark matter halo density profile in Fourier space (as a function of wavenumber k and redshift z for a given value of mass M) and $n_{\rm gal}$ is the mean number of galaxies per unit comoving volume at redshift z:

$$n_{\rm gal}(z) = \int dM\, \frac{dn_{\rm halo}}{dM}(z)\left[1 + \left(\frac{M}{M_1}\right)^{\alpha}\right]. \tag{11}$$

For the dark matter halo density function we adopt the Navarro-Frenk-White[44] profile truncated at the virial radius $r_{\rm vir}$ and with a concentration parameter given by:

$$c(M,z) = \frac{9}{1+z}\left(\frac{M}{M_*}\right)^{-0.13}; \tag{12}$$

here M_* is the characteristic mass scale at which the critical density required for spherical collapse is equal to the square root of the variance in the initial density field $\sigma(M)$ when extrapolated at the present time using linear theory such that $\delta_{\rm sc}(z) = \sigma(M_*)$, where $\delta_{\rm sc}(z) = 1.68/g(z)$, where $g(z)$ is the linear theory growth function for density perturbations.

As outlined above $M_{\rm min}$ determines both the one-halo and two-halo amplitudes, while α determines primarily the amplitude of the one-halo term and the overall number density of galaxies, which in return is connected to the amplitude of the two halo term via the halo bias factor. While with the two-halo term alone all these parameters are degenrate with each other and the bias factor, allowing only an average mass scale to be determined based on the bias factor, with one-halo term also included some of the degeneracies are broken and $M_{\rm min}$ and α can be determined independent of bias[18].

In the Limber approximation, the measured power spectrum of fluctuations can be expressed as the 2 dimensional, flux averaged projection of the three-dimensional galaxy power spectrum $P(k,z)$ as:

$$P(k_\theta) = \int_{z_{\rm min}}^{z_{\rm max}} P\left(k = \frac{2\pi\, k_\theta}{x(z)}, z\right)\left(\frac{d\mathcal{S}}{dz}(z)\right)^2 \frac{1}{dV_{\rm c}(z)}dz; \tag{13}$$

here $d\mathcal{S}/dz$ is the redshift distribution of the cumulative flux contributed by the background faint galaxies, $dV_{\rm c}$ is the comoving volume element, defined as $dV_{\rm c} \equiv x(z)^2 \frac{dx}{dz}$ and $x(z)$ is the comoving radial distance.

In this paper we determine the redshift distribution of the intensity by binning the redshift range in four redshift bins between $z = 0$ and $z = 4$ and putting constraints on $d\mathcal{S}/dz$ in each bin; the advantage of this approach is that we don't assume a particular model for $d\mathcal{S}/dz(z)$; instead, we let the data decide which model is more adequate.

The method we use to constrain our parameters is based on a modified version of the publicly available Markov-Chain Monte-Carlo (MCMC) package CosmoMC[45], with a convergence diagnostics based on the Gelman-Rubin criterion[46]. We consider a halo model described by the following set of parameters:

$$\{dS/dz_i, M_{\rm min}, \alpha, M_1, P_{\rm SN}\}\,, \tag{14}$$

where, as discussed before, we bin the cumulative flux $dS/dz(z)$ in four redshift bins, $dS/dz_i(z)$ $(i = 1, 2, ..4)$, representing the value at four redshift intervals, $\mathrm{bin}_i \in [0-1, 1-2, 2-3, 3-4]$. In the above $P_{\rm SN}$ is the shot-noise amplitude which we remeasure again for the halo model fits. To obtain

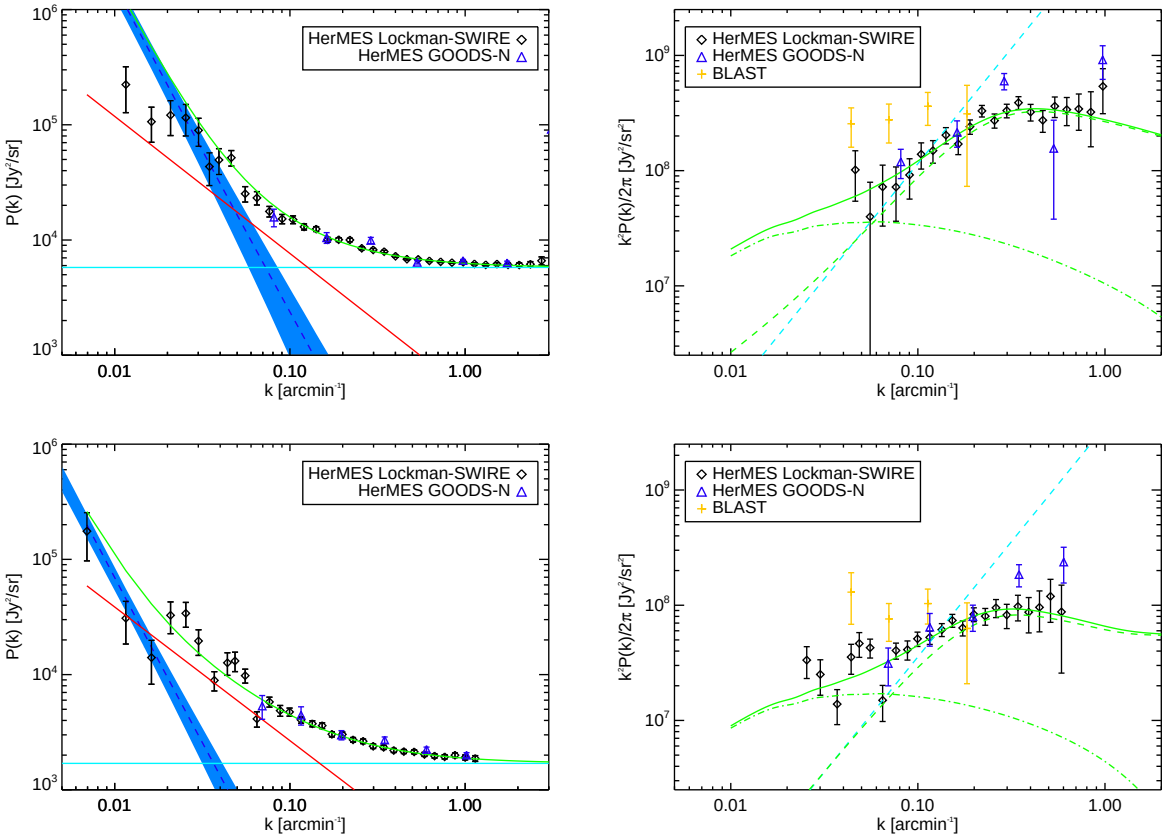

Figure S 10: **The fluctuation power spectrum and the clustering component.** The total power spectrum $P(k)$ (left panels) and clustering $P(k)$ with shot-noise removed (right panels) at 250 μm (top) and 500 μm (bottom), respectively. The power spectrum measurements shown are binned logarithmically for $k > 0.03$ arcmin^{-1}, with a bin width equal to $\Delta k/k = 0.15$, and linearly for smaller k, with a bin width of $\Delta k = 4.6 \times 10^{-3}$ arcmin^{-1}. This figure is similar to Fig 1.

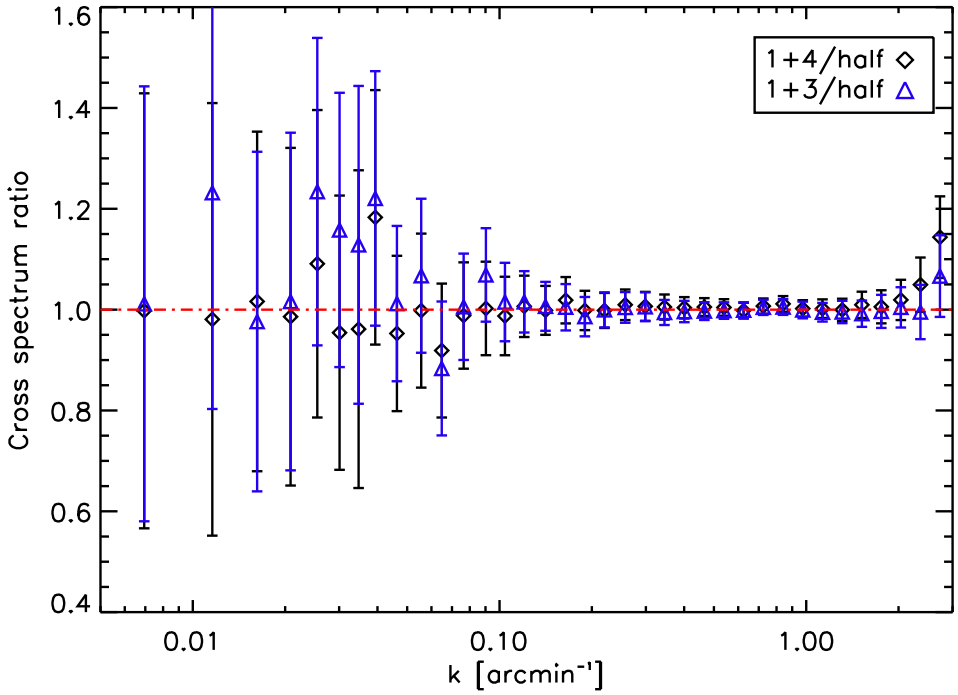

Figure S 11: **Accuracy of the power spectrum measurement.** Ratios of the total power spectra $P(k)$ estimated with different sub-maps of Lockman-SWIRE data normalized to the default power spectrum shown in the main paper estimated with the $(1+2)$ map cross-correlated against the $(3+4)$ map, after the data are divided into four sequential intervals in time, labeled 1 to 4, of equal duration. The 1 and 3 subsets have the same scan direction and the 2 and 4 subsets have the same scan directions, but the two subsets are almost orthogonal.

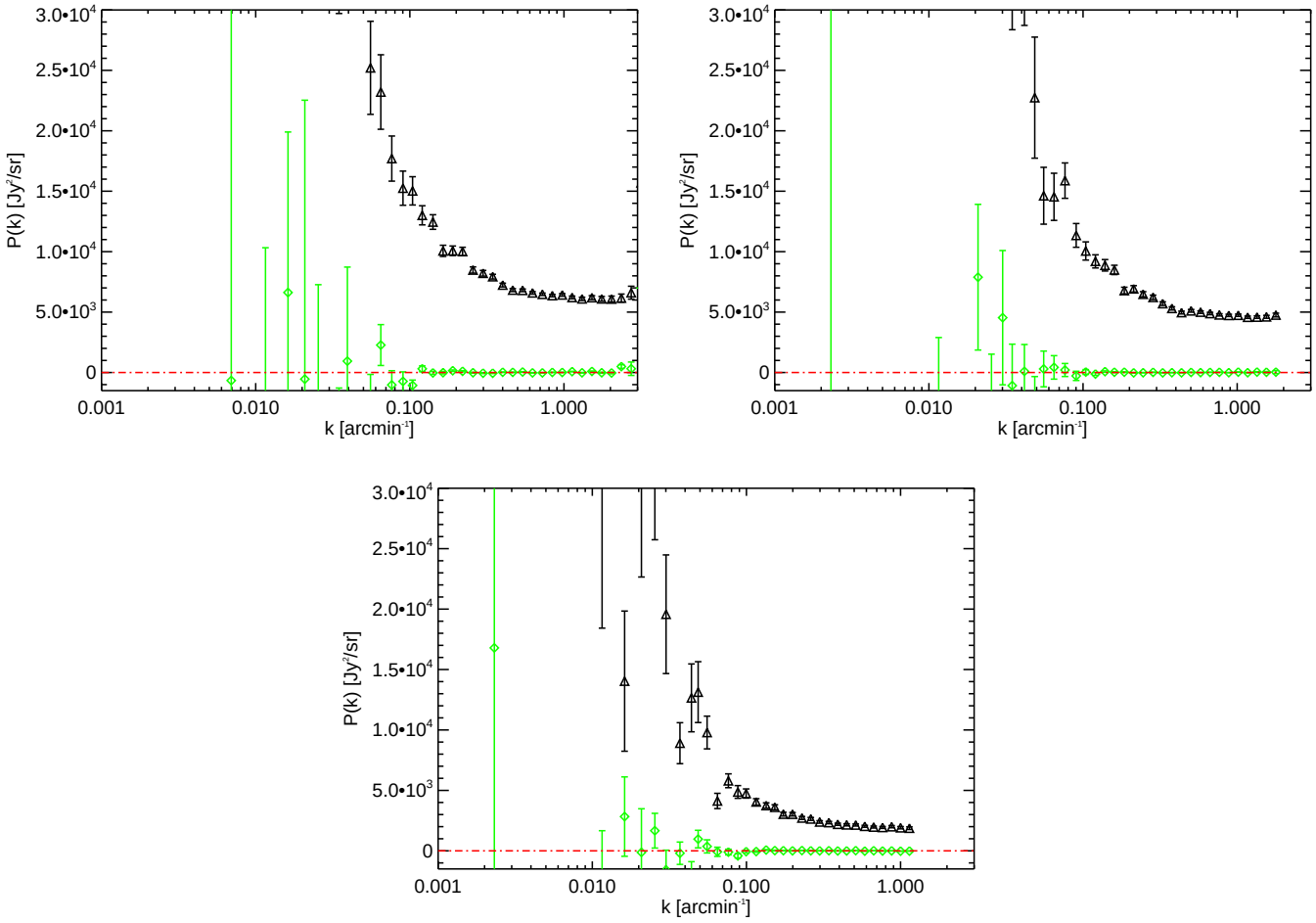

Figure S 12: **The null-test of the power spectrum measurement.** $P(k)$ measured (black triangle) on Lockman-SWIRE with the cross spectrum $[(1+2)\times(3+4)]$ at 250, 350, 500 μm (left to right, top to bottom). Cross power spectrum (green diamond) of the difference $[(1-2)\times(3-4)]$.

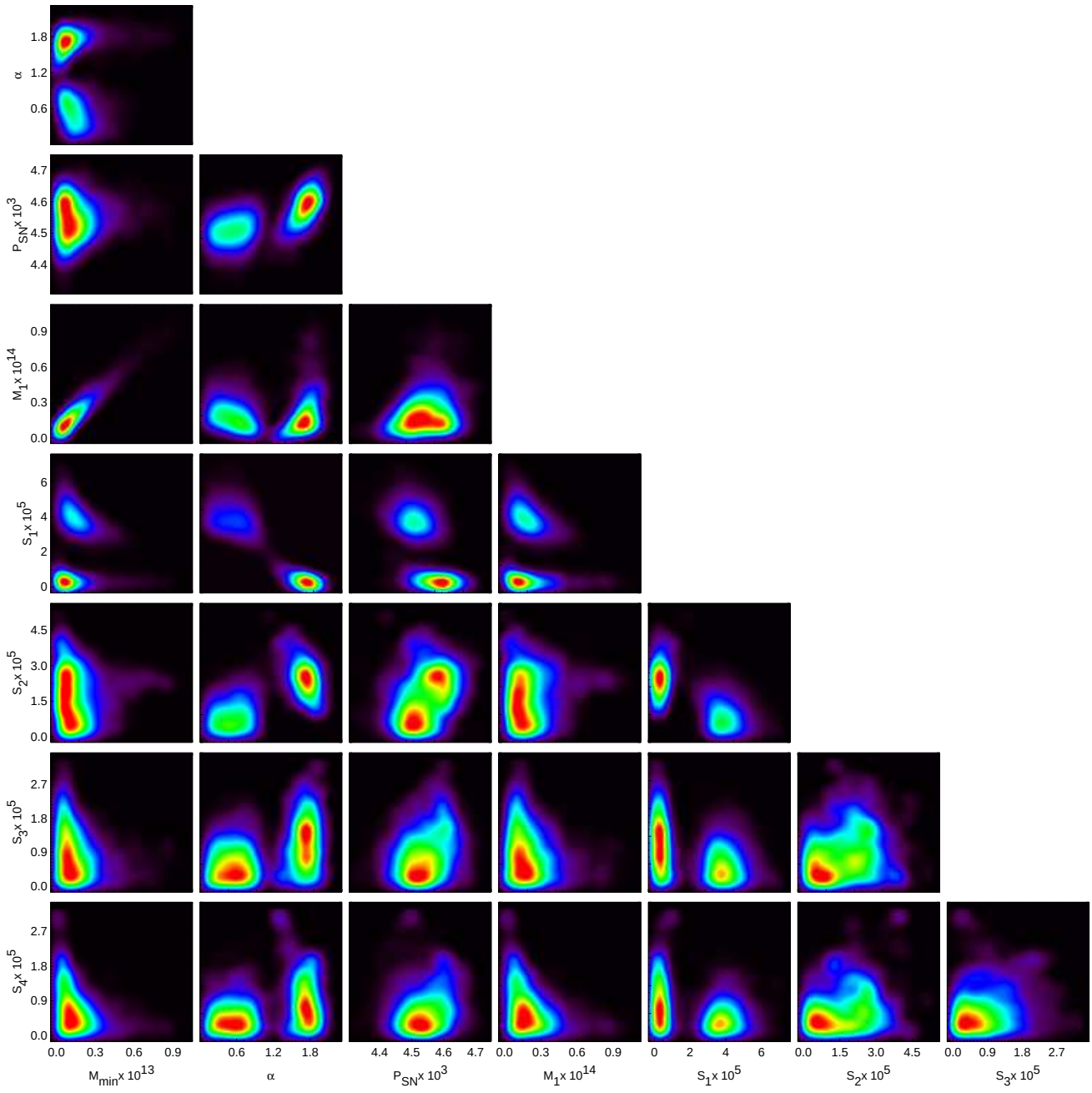

Figure S 13: **The halo model parameter estimates.** Bi-dimensional probability distribution function for all the pairs associated with our halo model fits with eight parameters ($M_1, M_{min}, \alpha, P_{SN}, S_1, S_2, S_3$ and S_4) showing our constraints and the degeneracies between the parameters. Here we show results at 350 μm, but degeneracies of parameters related to 250 and 500 μm model fits are similar.

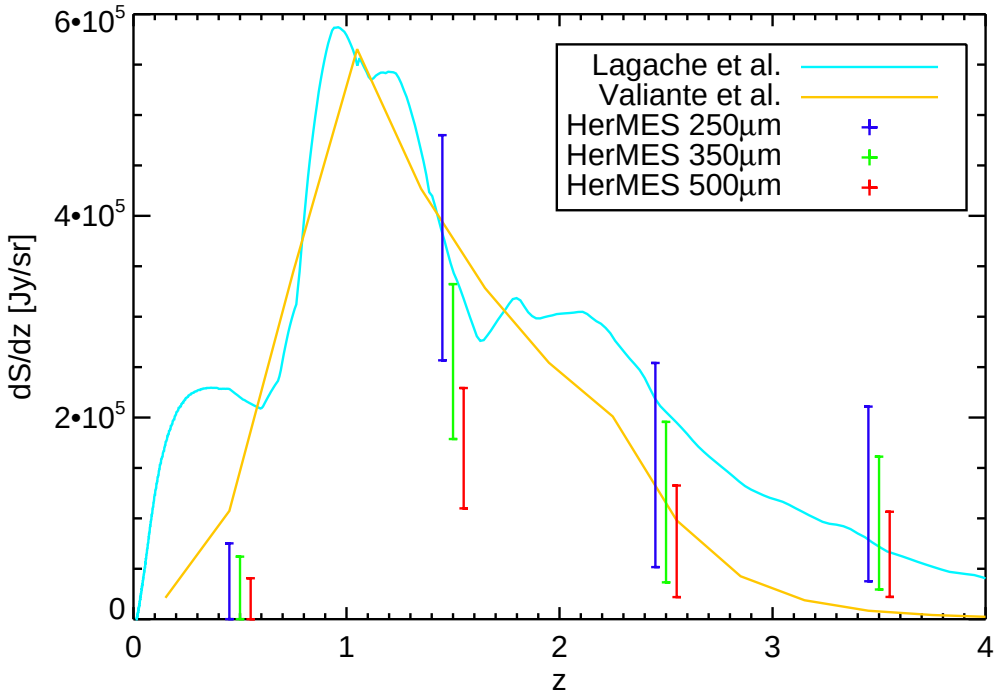

Figure S 14: **Redshift evolution of the galaxy intensities at the sub-millimetre wavelengths.** $d\mathcal{S}/dz$ as a function of redshift for 4 bins in redshift and for the three wavebands of SPIRE with $S < 50$ mJy. For reference, we show 2 model predictions from Lagache et al.[37] and Valiante et al.[38] for the same flux cut. We have used a prior on the occupation number slope $\alpha > 1$.

reliable model-fits to data we set a broad uniform prior on the ratio $M_1/M_{\rm min}$ to be between 10 to 25, consistent with numerical simulations of the halo occupation distribution which finds a value close to 15 for this ratio[47]. We also require that the redshift integrated source intensity be within the 68% confidence level ranges of the background light intensities as obtained by FIRAS[48]. The central values and errors we use are 0.85 ± 0.08, 0.65 ± 0.19 and 0.39 ± 0.10 MJy/sr at 250, 350, and 500 μm, respectively. For background cosmology, we assume the concordance model[49]. Our results related to the halo model fits are summarized in Table S3.

In comparison to the shot-noise values from model fits to the power spectrum (Table S2 for the power-law case and Table S3 for the halo model case), the shot-noise values from the best determined source counts[50] give 6900 ± 320, 4500 ± 220, and 1600 ± 100 Jy^2/sr at 250, 350, and 500 μm, respectively.

In Figure S13 we show the two-dimensional constraints on pairs of parameters that highlight the degeneracies associated with this eight parameter model fit. The best-fit values and the errors at each of the three wavebands are show in Figure S14.

Additionally, we compute the far-infrared bolometric luminosity between 8 and 1100 μm in each of the redshift bins from the $dS/dz(z)$ values by modelling the flux received between a redshift $z^i_{\rm min}$ and $z^i_{\rm max}$ in each j SPIRE bands, defined by the bandpass $f_j(\nu)$:

$$dS^j/dz^i = L_{\rm FIR}\int_{z^i_{\rm min}}^{z^i_{\rm max}} dz \frac{(1+z)^{(\beta+1)}}{4\pi D_L^2(z)} \frac{\int \nu^\beta B(\nu(1+z),T) f_j(\nu) d\nu}{\int_{270\,{\rm GHz}}^{38\,{\rm THz}} \nu^\beta B(\nu,T) d\nu} \quad (15)$$

The temperature T is chosen to be 28 ± 8 K and the emissivity index β is fixed to 1.5, we then fit for $L_{\rm FIR}$ given the measured values and the predicted values of dS/dz_i. The temperature uncertainty is incorporated into the $L_{\rm FIR}$ error budget. We summarize our results related to $L_{\rm FIR}$ as a function of redshift in Figure 2. $L_{\rm FIR}$ is a measure of the star-formation rate with[51]

$$\mathrm{SFR}[\mathrm{M}_\odot \mathrm{yr}^{-1}] = 1.73\times10^{-10}\, L[\mathrm{L}_\odot]\,. \quad (16)$$

We use this to also show the SFR implied by $L_{\rm FIR}$ in Figure 2. Here we have subselected the models that lead to $\alpha > 1$ to be consistent with the occupation numbers at other wavelenegths[41,42]. $L_{\rm FIR}$ as a function of redshift has been predicted in two analytical models of sub-millimetre galaxy population[37,38] and we make a comparison in the same figure.

References:

31. Ott, S. 2010, in Astronomical Data Analysis Software and Systems XIX, ed. Y.Mizumoto, K.-I. Morita, and M. Ohishi, ASP Conf. Series.

32. Levenson, L. et al. 2010, Mon. Not. R. Astron. Soc. in press, arXiv.org:1010.0020

33. Swinyard, B. et al. In-flight calibration of the Herschel-SPIRE instrument, Astron. Astrophys. 518, L4 (2010).

34. Fixsen, D.J., Moseley, S.H. & Arendt, R.G. Calibrating Array Detectors, Astrophys. J. Supp. 128, 651-658 (2000).

35. Hivon, E. et al. MASTER of the Cosmic Microwave Background Anisotropy Power Spectrum: A Fast Method for Statistical Analysis of Large and Complex Cosmic Microwave Background Data Sets. Astrophys. J. 567, 2-17 (2002).

36. Knox, L., Phys. Rev. D., 52, 4307-4318 (2005).

37. Lagache, G., Dole, H. & Puget, J.-L. Modelling the infrared galaxy evolution using a phenomenological approach, Mon. Not. R. Astron. Soc. 338, 555-571 (2003).

38. Valiante, E. et al. A Backward Evolution Model for Infrared Surveys: The Role of AGN- and Color-$L_{\rm TIR}$ Distributions. Astrophys. J. 701, 1814-1838 (2009).

39. Lagache, G. Bavouzet, N., Fernandez-Conde, N. et al. Correlated Anisotropies in the Cosmic Far-Infrared Background Detected by the Multiband Imaging Photometer for Spitzer: Constraint on the Bias. Astrophys. J. 665, L89-L92 (2007).

40. Schlegel, D. J., Finkbeiner, D. P., Davis, M. Maps of Dust Infrared Emission for Use in Estimation of Reddening and Cosmic Microwave Background Radiation Foregrounds. Astrophys. J. 500, 525-534 (1998).

41. Cooray, A., Sheth, R. Halo models of large scale structure. Phys. Rep. 372, 1-129 (2002).

42. Zehavi I., et al. Astrophys. J., 630, 1-27 (2005).

43. Sheth, R. K., Mo, H. J., Tormen, G. Ellipsoidal collapse and an improved model for the number and spatial distribution of dark matter haloes. Mon. Not. Roy. Astron. Soc. 323, 1-12 (2001).

44. Navarro, J. F., Frenk, C. S., White, S. D. M. A Universal Density Profile from Hierarchical Clustering. Astrophys. J. 490, 493-510 (1997).

45. Lewis, A. & Bridle, S. Cosmological parameters from CMB and other data: A Monte Carlo approach. Phys. Rev. D. 66, 103511 (2002).

46. Gelman, A., Rubin, D. B. Inference from iterative simulation using multiple sequencies. Statistical Science. 7, 457-472 (1992).

47. Zheng, Z. et al. Theoretical Models of the Halo Occupation Distribution: Separating Central and Satellite Galaxies, ApJ, 633, 791-809 (2005).

48. Fixsen, D. J., Dwek, E., Mather, J. C., Bennett, C. L. & Shafer, R. A. The spectrum of the extragalactic far-infrared background from the COBE FIRAS observations. Astrophys. J. 508, 123-128 (1998).

49. E. Komatsu et al. Seven-Year Wilkinson Microwave Anisotropy Probe (WMAP) Observations: Cosmological Interpretation, Astrophys. J. Supp. submitted, arXiv.org:1001.4538 (2010).

50. Glenn, J. et al. HerMES: Deep Galaxy Number Counts from a P(D) Fluctuation Analysis of SPIRE Science Demonstration Phase Observations, Mon. Not. R. Astron. Soc. in press, arXiv.org:1009.5675 (2010).

51. Kennicutt, R. C. Jr. Star Formation in Galaxies Along the Hubble Sequence, Ann. Rev. of Astron. Astrophys. 36, 189-232 (1998).